Log-Gabor Filters for Image-Based Vehicle Verification

Jon Arróspide and Luis Salgado

***Abstract*— Vehicle detection based on image analysis has attracted increasing attention in recent years due to its low cost, flexibility, and potential toward collision avoidance. In particular, vehicle verification is especially challenging on account of the heterogeneity of vehicles in color, size, pose, etc. Image-based vehicle verification is usually addressed as a supervised classification problem. Specifically, descriptors using Gabor filters have been reported to show good performance in this task. However, Gabor functions have a number of drawbacks relating to their frequency response. The main contribution of this paper is the proposal and evaluation of a new descriptor based on the alternative family of log-Gabor functions for vehicle verification, as opposed to existing Gabor filter-based descriptors. These filters are theoretically superior to Gabor filters as they can better represent the frequency properties of natural images. As a second contribution, and in contrast to existing approaches, which transfer the standard configuration of filters used for other applications to the vehicle classification task, an in-depth analysis of the required filter configuration by both Gabor and log-Gabor descriptors for this particular application is performed for fair comparison. The extensive experiments conducted in this paper confirm that the proposed log-Gabor descriptor significantly outperforms the standard Gabor filter for image-based vehicle verification.**

***Index Terms*— Gabor filter, hypothesis verification, intelligent vehicles, log-Gabor filters, machine learning.**

I. Introduction

THE increasing interest on advanced driver assistance systems (ADAS) for the improvement of road safety has been reflected in the joint involvement of universities, research centers and car manufacturers, as well as in the deployment of national and international projects to address this issue. According to statistics, most of the accidents are caused by other cars, therefore vehicle detection arises as the key challenge for ADAS. In particular, the research on approaches based on image analysis for vehicle detection is gaining interest on account of its low cost and flexibility, and of the increased processing capabilities.

A very complete survey of image-based vehicle detection can be found in [1]. Most of the reported methods address vehicle detection in two stages, namely hypothesis generation and hypothesis verification. In the former, a quick search is performed so that potential locations of the vehicles in the image are hypothesized. The search is typically based on some expected feature of vehicles, such as color [2], [3], shadow [4], [5], vertical edges [6], or motion [7]. The aim of the second stage is to verify the correctness of the vehicle candidates provided by the hypothesis generation stage.

Traditionally, fixed [8] or deformable [9] models have been used for vehicle verification, However, the increase of processors speed in the last years has enabled the use of learning-based methods for real-time vehicle verification. In particular, this is usually addressed as a two-class supervised classification problem in which a set of samples are trained in search of specific feature descriptors of the vehicle and the nonvehicle classes. Some widespread descriptors include Gabor filters, principal component analysis (PCA) [10], and histograms of oriented gradients (HOG) [11], [12].

In particular, Gabor filters have been broadly used for image-based vehicle verification [13]–[16]. Traditionally, a Gabor filter bank at different scales and orientations is used for feature extraction. For instance, in [15], a bank of 8 Gabor filters with 2 different wavelengths and 4 different orientations is used. In [14], Gabor filter performance is analyzed for two different configurations, using 3 scales and 5 orientations, and 4 scales and 6 orientations, respectively.

The response of each filter in the bank is typically represented by statistics such as the mean and the standard deviation, both for characterization of vehicles [13], [17] or other objects [18]–[20]. These statistics can be extracted over the whole image [18], [19] or in smaller subwindows [21]. For instance, in [14] the candidate image is divided into nine overlapping sub-windows. Alternatively, in [15], seven Hu's invariant moments [22] are derived to build the feature vector. Other representations of texture based on Gabor filters are analyzed in [23].

Although Gabor filters have been extensively applied for a broad range of applications, they involve a number of drawbacks. First, the bandwidth of a Gabor filter is typically limited to one octave (otherwise it yields a too high DC component), thus a large number of filters is needed to obtain wide spectrum coverage. In addition, as suggested in [24], the

Manuscript received August 10, 2012; revised December 17, 2012; accepted February 4, 2013. Date of publication February 26, 2013; date of current version April 12, 2013. This work was supported by the Ministerio de Industria, Energía y Turismo of the Spanish Government under Project TEC2010-20412 (Enhanced 3DTV) and Project TEC2007-67764 (SmartVision). The associate editor coordinating the review of this manuscript and approving it for publication was Prof. Carlo S. Regazzoni.

J. Arróspide was with the Grupo de Tratamiento de Imágenes, E.T.S.I. Telecomunicación, Universidad Politécnica de Madrid, Madrid 28040, Spain. He is now with Altran Spain, Methods & Tools, Madrid 28022, Spain (e-mail: jal@gti.ssr.upm.es).

L. Salgado is with the Grupo de Tratamiento de Imágenes, E.T.S.I. Telecomunicación, Universidad Politécnica de Madrid, Madrid 28040, Spain, and also with the Video Processing and Understanding Laboratory, Universidad Autónoma de Madrid, Madrid 28049, Spain (e-mail: L.salgado@gti.ssr.upm.es).

Color versions of one or more of the figures in this paper are available online at http://ieeexplore.ieee.org.

Digital Object Identifier 10.1109/TIP.2013.2249080

amplitude of natural images (defined as the square root of the power spectrum) falls off in average by a factor of roughly $1/f$. This is in contrast to the properties of Gabor filters: on the one hand, a big extent of the Gabor response concentrates on the lower frequencies, which in turn results in redundant information of the filters; on the other hand, the high frequency tail of the images is not captured.

In this paper, an alternative representation of images for vehicle classification using log-Gabor filters [24] instead of Gabor filters is proposed and evaluated. Log-Gabor filters are designed as Gaussian functions on the log axis, which is in fact the standard method for representing the spatial-frequency response of visual neurons. Their symmetry on the log axis results in a more effective representation of the uneven frequency content of the images: redundancy in lower frequencies is reduced, and the response of the filter in the linear frequency axis displays a tail in the higher frequencies that adapts the frequency fall-off of natural images. Furthermore, log-Gabor filters do not have a DC component, which allows an increase in the bandwidth, and hence fewer filters are required to cover the same spectrum.

The main contribution of this paper is the design of a descriptor based on log-Gabor functions for vehicle verification instead of state-of-the-art descriptors based on Gabor functions. To our knowledge these functions have not been previously used for vehicle representation purposes. The purpose of this study is thus to experimentally demonstrate the referred theoretical superiority of log-Gabor filters over standard Gabor filters in this field.

Additionally, an in-depth analysis of the required filter bank configuration in the particular field of vehicle imaging is performed both for Gabor filters and log-Gabor filters. Indeed, a shortcoming of the existing works in the vehicle classification through Gabor filters is that they mirror the standard configurations of Gabor filters proposed by pioneering papers, even if those are devoted to general applications. For instance, many authors resort to the four-scale and six-orientation scheme proposed by [19] for texture retrieval. The analysis performed allows to maximize the accuracy of both Gabor and log-Gabor based descriptors and to compare the performance of the proposed log-Gabor filters with respect to the state-of-the art Gabor filter based approach under a fair and optimal reference framework.

This paper is organized as follows. In Sections II and III the fundamentals of Gabor and log-Gabor filters are respectively reviewed. Section IV provides details on the filter bank configuration and on feature extraction. Section V provides an exhaustive analysis of the performance of the Gabor filter based descriptor. Finally, in Section VI, extensive experiments are enclosed measuring the performance of the proposed log-Gabor function based descriptor, and comparing it to state-of-the-art Gabor filter based approach and to other related methods. Experiments show that log-Gabor filters significantly outperform traditional Gabor filters for vehicle verification.

II. Review on Gabor Filters

Two-dimensional Gabor functions are composed of a complex sinusoidal carrier and a Gaussian envelope. The Fourier transform of $g(x, y)$ is given by

$$G(u, v) = \exp\left\{-\frac{1}{2}\left[\frac{(u - F_0)^2}{\sigma_u^2} + \frac{v^2}{\sigma_v^2}\right]\right\}. \quad (1)$$

Remarkably enough, Daugman [25] found that this family of Gabor functions describes well the 2D receptive-field profile of simple cells in mammalian visual cortex. Therefore, the perception of the human visual system can be emulated through image analysis using these functions. This has motivated the use of Gabor filters for a broad spectrum of applications including image compression [26], browsing and retrieval of image data [18], [19], segmentation [27], [28], texture classification [20], [29], and [30], object tracking [31] and feature extraction for further classification [15], [17], and [32]. They are in all cases tightly related to the texture analysis of the image.

A Gabor filter provides a localized frequency description. Hence, in order to capture all the frequency content of a certain texture pattern, a bank of filters in different frequencies is needed. Let $g(x, y)$ be the mother generating function for the Gabor filter family. Then, we shall create a set of functions, denoted $g_{m,n}(x, y)$, by appropriately rotating and scaling $g(x, y)$:

$$g_{m,n} = a^{-2m} g(x', y') \quad (2)$$

where $x' = a^{-m}(x\cos\theta_n + y\sin\theta_n)$, $y' = a^{-m}(-x\sin\theta_n + y\cos\theta_n)$, and $a > 1$. Let us consider a bank of filters with N different scales and K orientations, thus it is $m = 0, \ldots, N-1$ and $n = 0, \ldots, K-1$. Observe that each filter describes a frequency $F_m = a^{-m}F_0$ and an angle $\theta_n = n\pi/K$. The corresponding Fourier transform of such a filter in Cartesian coordinates is [33]

$$G_{m,n}(u, v) = \exp\left\{-\frac{1}{2}\left[\frac{(u-u_{m,n})_r^2}{a^{-2m}\sigma_u^2} + \frac{(v-v_{m,n})_r^2}{a^{-2m}\sigma_v^2}\right]\right\} \quad (3)$$

where $(u_{m,n}, v_{m,n})$ are the spatial frequencies of the sinusoidal carrier, i.e., $u_{m,n} = F_m\cos\theta_n$, $v_{m,n} = F_m\sin\theta_n$, and r indicates rotation so that

$$\begin{aligned}(u - u_{m,n})_r &= (u - u_{m,n})\cos\theta_n + (v - v_{m,n})\sin\theta_n \\ (v - v_{m,n})_r &= -(u - u_{m,n})\sin\theta_n + (v - v_{m,n})\cos\theta_n. \end{aligned} \quad (4)$$

Fig. 1 illustrates the frequency response of the Gabor filter bank. Gabor functions form a complete but nonorthogonal basis, which implies that there is some degree of redundancy in the filters responses. This redundancy is minimized following the same criterion as in [18], which imposes that the half-peak magnitude contours of the filter responses in the frequency domain be tangent to each other. As shown in [18], the parameters σ_u and σ_v are then given by $\sigma_u = ((a-1)F_0/(a+1))\sqrt{2\ln 2}$ and $\sigma_v = \tan(\pi/2K)\sqrt{(F_0^2/2\ln 2) - \sigma_u^2}$.

III. Log-Gabor Filters

As stated in Section I, the properties of Gabor filters involve two important drawbacks. On the one hand, their bandwidth must be limited in order to prevent a too high DC component. Hence, a larger number of filters is needed to cover the desired spectrum. On the other hand, their response is symmetrically distributed around the center frequency, which

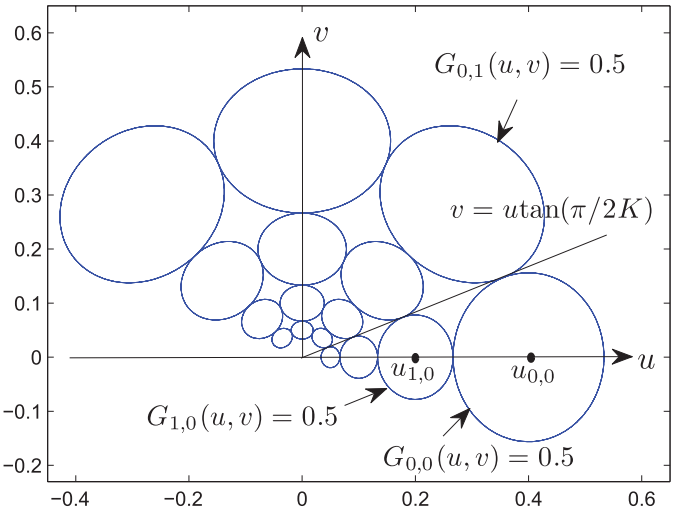

Fig. 1. Frequency response of the Gabor filter bank. The contours indicate the half-peak magnitude of the filter responses in the Gabor filter family. The filter parameters used here are $K = 4$, $N = 4$, $a = 2$, and $F_0 = 0.4$.

results in redundant information in the lower frequencies that could instead be devoted to capture the tails of images in the higher frequencies.

An alternative to the Gabor filters is the log-Gabor function introduced by Field [24]. The frequency response of log-Gabor filters in polar coordinates is given by [34]

$$LG_{m,n}(f,\theta) = \begin{cases} \exp\left\{-\frac{(\log(f/F_m))^2}{2(\log\beta)^2}\right\} \exp\left\{-\frac{(\theta-\theta_n)}{2\sigma_\theta^2}\right\} & f \neq 0 \\ 0 & f = 0. \end{cases} \quad (5)$$

It is also common to find in the literature their corresponding expression in the log axis [35]:

$$LG_{m,n}(\rho,\theta) = \exp\left\{-\frac{(\rho-\rho_m)^2}{2\sigma_\rho^2}\right\} \exp\left\{-\frac{(\theta-\theta_n)^2}{2\sigma_\theta^2}\right\} \quad (6)$$

where $\rho = \log f$, $\rho_m = \log F_m$, $\sigma_\rho = \log\beta$ and $f \neq 0$. The parameter β determines the bandwidth of the filter. For instance, a value of $\beta = 0.75$ results in an approximate bandwidth of one octave, whereas $\beta = 0.55$ extends roughly as far as two octaves [36]. The angular bandwidth, σ_θ, is typically set to approximately 1.5 for even spectrum coverage.

As can be observed in (6), log-Gabor functions are symmetrical in the log-axis instead of the linear frequency axis, which yields a more effective representation of images. Indeed, they feature a tail in the higher frequencies of the linear axis that is in line with the amplitude fall-off of natural images. In turn, redundancy in the lower frequencies is reduced, thus achieving a more efficient coverage of the frequency spectrum. In addition, as shown in (5), the DC-component of log-Gabor filters is zero by definition, hence the bandwidth of each filter in the bank can be enlarged and the overall number of required filters can be reduced with respect to standard Gabor filters.

IV. Design of the Descriptor

Prior to defining the Gabor and log-Gabor descriptors, let us make some considerations related to the filtering process.

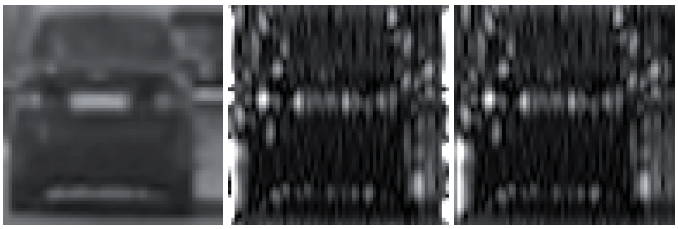

Fig. 2. Effect of circular convolution. (a) Original image. (b) Gabor-filtered image with circular convolution. Observe the artifacts produced in the image boundaries due to luminance discontinuity. (c) The result after replicating the image boundaries prior to filtering (the image is cropped to the size of the original image), in which artifacts have been removed.

Naturally, the input space is discrete, therefore in order to transfer the image (of size $R \times C$) and the filter to the frequency domain, the Discrete Fourier Transform (DFT) is required. The filtered image in the input space is eventually obtained by applying the Inverse DFT (IDFT) to the product of the image and the filter in the frequency domain. At this point it is interesting to recall that the product of DFTs is equivalent to the circular convolution of the corresponding functions in the spatial domain. Thus, the discontinuity between the intensity in the different borders of the original image affects the filtering and produces artifacts in the output image contour. This is illustrated in Fig. 2 for a given example image: the result of the application of a Gabor filter of parameters $F_0 = 0.4$, $\sigma_x = \sigma_y = 1/2F_0$, $\theta_0 = 0°$ over the image in Fig. 2(a) is shown in Fig. 2(b). Since the filter is oriented in the horizontal axis, artifacts arise in the left and right boundaries of the image.

In order to avoid this effect in both Gabor and log-Gabor filtering, we propose to enlarge the original image by replicating its boundaries (i.e., values outside the bounds of the image are assumed to equal the nearest border value). The artificially imposed continuity at the borders results in a low response to the filter, while the artifacts due to circular convolution are shifted to the new image boundaries. Those are conveniently discarded after obtaining the filtered image through the IDFT. The size of the enlarged image is $(R + E) \times (C + E)$, where E must be greater than the width of the filter envelope, $E > \sigma_x$, $E > \sigma_y$. The application of the same filter described above on the enlarged image results in the image shown in Fig. 2(c), where appropriate cropping has been performed: the artifacts are no longer observed in the borders.

In addition, in our study Gabor filters have been forced to have a zero DC component by setting $G_{m,n}(0,0) = 0$, as done in other approaches to Gabor filtering [19], [30], in order to reduce the sensitivity of the filter to absolute intensity values.

A. Feature Extraction

Several strategies can be taken to define the feature vector from the result of Gabor filtering. Some of them are discussed in [23] and include the use of raw Gabor responses, thresholded Gabor features, Gabor energy features and grating cell operator features. These are compared in [23] in a set of generic texture images based on the Fisher criterion. The former two deliver poor results, whereas good performance is

achieved by Gabor energy features and grating cell operator features. However, the latter are not suited for vehicle classification, as they require that a system of at least three bars is present in their receptive fields [23]. Gabor energy features (which combine the response of symmetric and antisymmetric Gabor filter) are thus selected. These features result in very large vectors (as large as the size of the image) and thus entail heavy training and classification. Therefore, statistical moments are usually preferred [17]–[19], [32], and will also be adopted in this paper. In particular, three moments are analyzed: the mean, μ, the standard deviation, σ, and the skewness, γ, of the data distribution:

$$\mu_{m,n} = \frac{1}{R \cdot C} \sum_x \sum_y \left| J_{m,n}(x,y) \right|$$

$$\sigma_{m,n} = \sqrt{\frac{1}{R \cdot C} \sum_x \sum_y (\left| J_{m,n}(x,y) \right| - \mu_{m,n})^2}$$

$$\gamma_{m,n} = \frac{1}{R \cdot C} \sum_x \sum_y \left(\frac{\left| J_{m,n}(x,y) \right| - \mu_{m,n}}{\sigma_{m,n}} \right)^3 \quad (7)$$

where $J_{m,n}(x,y)$ represents the input image $I(x,y)$ filtered by one of the filters in the Gabor filter bank, $G_{m,n}$, or the log-Gabor bank, $LG_{m,n}$, and $|\cdot|$ denotes the modulus of a complex number. The mean and the variance are deemed essential and are therefore always included in the feature vector. The skewness, in turn, may be included if the gain in performance justifies the computational overhead. To assess the amount of information conveyed by this parameter, let us analyze its distribution along the Gabor-filtered images. Specifically, a reference Gabor filter bank with parameters $N = 4$, $K = 6$, $F_0 = 0.4$, and $a = 2$ is selected, and the skewness is computed for each filtered image. These values are computed for all the vehicle and nonvehicle images of a public database (this is described in Section VI), broken down by regions. As a result, the histograms shown in Fig. 3 are obtained. As can be observed, the profiles of vehicle and nonvehicle instances are fairly similar for all regions, which suggests that this parameter is not meaningful for class separation.

The feature vector is thus composed of the mean and variance of the images resulting of applying the Gabor or log-Gabor filter bank to the input image:

$$v \simeq \left[\mu_{0,0}, \sigma_{0,0}, \mu_{1,0}, \sigma_{1,0}, \ldots, \mu_{N-1,K-1}, \sigma_{N-1,K-1} \right]. \quad (8)$$

V. Performance of Gabor Filter-Based Classifier

In this section the performance of Gabor-filter based descriptor is analyzed as a function of several parameters. This represents the state of the art in the use of this technique for the vehicle verification task (e.g., [13]–[15]). The objective is to find the configuration which exploits their full potential so that proper comparison with the log-Gabor based descriptor proposed in this paper can be performed (this is addressed in Section VI).

A. Experimental Setup

The methodology for the experiments is as follows. Regarding the classification procedure, the feature vector extracted for the descriptors is fed to a Support Vector Machine (SVM) classifier. These classifiers are extensively used in the related literature owing to their good generalization, and have been reported to deliver better performance than other traditional methods, e.g. Neural Networks (see [14]). Hence, linear SVMs are also used as baseline classifiers for descriptor comparison in this paper. However, the selection of an optimal classifier is out of the scope of this paper, as the core of the paper is in the design of an effective descriptor to discriminate between vehicles and nonvehicles.

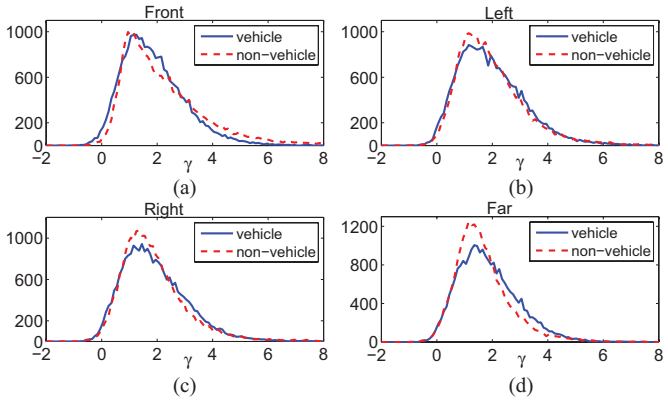

Fig. 3. Histogram of skewness along Gabor-filtered images throughout the image database for the two classes (vehicle, nonvehicle) and the four regions.

Regarding the data set, the open access GTI vehicle image database [37] is used for the experiments. This data set consists of 4000 positive images of vehicle rears and 4000 negative images of other elements in traffic sequences. Monochrome images are used as the proposed descriptors pertain to texture rather than color. The images are divided in four different groups according to the relative pose of the vehicle with respect to the camera (close/middle range in the front, in the left and in the right, and far range), each of them comprising 1000 positive and 1000 negative images. Vehicle pose affects the imaging of the different vehicle elements and thus this division of the data set allows for the descriptors to account for vehicle pose by appropriately selecting the corresponding parameters for each image region. Sample vehicle images for the different regions are illustrated in Fig. 4. Observe the complexity of the vehicle/nonvehicle classification task due to the high variability of the samples in terms of shape, pose, size, vehicle type, etc.

The training and testing sets are generated by means of 5-fold 50% holdout cross-validation, that is, each experiment consists of five iterations, in each of which half of the samples are randomly chosen for training and the other half are used for testing. The result of the experiment is the average of all the iterations. The performance is measured in terms of accuracy, i.e., the proportion of correct predictions in the testing set population.

B. Experiments With Gabor Filter-Based Classifier

A set of simulations have been performed on the GTI vehicle database to derive the combination of parameters of the Gabor filter bank that yields best vehicle classification

Fig. 4. Examples of vehicle (left) and nonvehicle (right) samples contained in the GTI database. Each row comprises samples in the front close/middle region, the left close/middle region, the right close/middle region and the far region, respectively, from top to bottom. Note the differences between the vehicle samples in terms of color, shape, pose, size (due to camera location and perspective effect), and type of vehicle (car, van, truck, etc.), and the effect of illumination and weather conditions, which makes vehicle/nonvehicle discrimination highly challenging.

performance. These parameters comprise the number of scales, N, the number of orientations, K, the maximum frequency, F_0, and the scaling between center frequencies, a.

1) Performance as a Function of the Number of Scales: Once the final set of features has been defined, the next step is to evaluate the classification accuracy as a function of the number of scales and orientations. With regard to the former, the limited bandwidth of Gabor filters predicts a significant impact in the classification performance when the number of filters is decreased, since the frequency spectrum cannot be evenly covered. Accuracy is tested for $1 \leq N \leq 4$, and for each value of N several experiments are performed to find the appropriate F_0 (or more precisely its inverse, λ_0). The values tested for λ_0 have been chosen so that the bank covers roughly the range of frequencies $[0.05, 0.5]$ (or equivalently the range of wavelengths $[2, 20]$), which corresponds to the frequency content implicit in vehicle images, according to [14]. The scaling between center frequencies is also tuned to achieve this goal ($a = 2$ for $N = 4$ and $N = 3$, $a = 3$ for $N = 2$ and $N = 1$). For all tests the number of orientations is kept to $K = 6$. The results of these tests are enclosed in Table I. If the F_0 rendering the best performance is selected for each value of N, the accuracy rates shown in Table II are obtained.

To visualize these rates, the accuracy values are represented in Fig. 5 as a function of the number of scales of the filter bank. As can be observed, the performance decreases quasi-linearly from $N = 4$ to $N = 2$, and then falls more abruptly for $N = 1$. Quick inspection of Table I hints that, for a given N, the classification results have a different trend for the close/middle range than for the far range when varying λ_0. Specifically, the classifiers in the front, left and right close/middle ranges have a classification maximum for low λ_0 (i.e., high F_0), whereas the far range classifier displays better results for somewhat higher values of λ_0.

Let Fig. 6 graphically illustrate the rates in Table I. The figures for the close/middle range have been computed as the average of the front, left, and right rates. As expected, the solid lines corresponding to the close/middle range have their maximum at a lower λ_0 than their dual dashed lines at the far range for all values of N. This is not surprising, taking into account that in the far distances the images contain little detail and thus the edges and the frequency content are less sharp.

TABLE I
ACCURACY OF GABOR FILTERS AS A FUNCTION OF THE NUMBER OF SCALES

$N = 4$	$\lambda_0 = 2$	$\lambda_0 = 2.5$	$\lambda_0 = 3$	$\lambda_0 = 4$	$\lambda_0 = 5$
Front	97.70	97.46	97.62	97.46	96.98
Left	96.72	96.66	96.48	96.24	95.10
Right	96.56	96.04	96.40	95.92	94.98
Far	88.88	89.50	90.04	89.12	89.42
Mean	94.96	94.91	95.14	94.69	94.12

$N = 3$	$\lambda_0 = 2$	$\lambda_0 = 3$	$\lambda_0 = 4$	$\lambda_0 = 5$
Front	97.44	97.46	97.20	97.16
Left	95.98	95.90	95.84	96.04
Right	96.28	95.98	95.50	95.40
Far	86.62	88.18	88.58	89.24
Mean	94.08	94.38	94.28	94.46

$N = 2$	$\lambda_0 = 2$	$\lambda_0 = 4$	$\lambda_0 = 6$	$\lambda_0 = 8$
Front	96.62	95.90	95.42	94.12
Left	95.76	94.86	94.06	93.26
Right	95.28	94.60	94.14	93.42
Far	87.00	87.40	87.18	86.76
Mean	93.67	93.19	92.70	91.89

$N = 1$	$\lambda_0 = 1$	$\lambda_0 = 5$	$\lambda_0 = 10$	$\lambda_0 = 15$	$\lambda_0 = 20$
Front	90.84	94.98	94.06	91.52	90.50
Left	92.80	93.02	91.24	90.88	89.76
Right	88.76	92.98	91.46	91.26	91.06
Far	82.04	84.26	85.74	84.08	81.82
Mean	88.61	91.31	90.03	89.44	88.28

TABLE II
AVERAGE ACCURACY RESULTS OF GABOR FILTERS FOR DIFFERENT VALUES OF N FOR THE OPTIMAL FIXED λ_0

	$N = 4$	$N = 3$	$N = 2$	$N = 1$
Accuracy	95.14	94.46	93.67	91.31

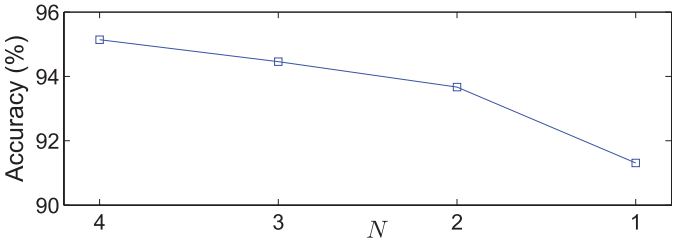

Fig. 5. Evolution of accuracy of Gabor filters as a function of N.

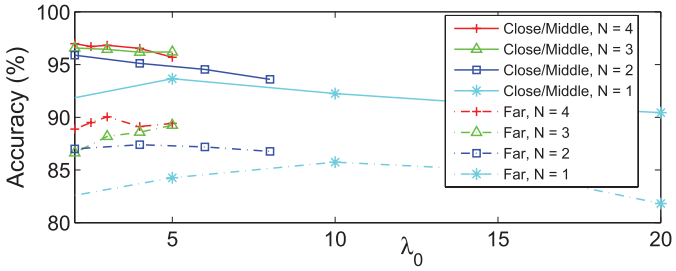

Fig. 6. Evolution of accuracy of Gabor filters as a function of the minimum wavelength λ_0 in the close/middle range (solid lines) and the far range (dashed lines).

TABLE III

VALUES OF λ_0 ADAPTED TO EACH IMAGE REGION FOR GABOR FILTER PERFORMANCE MAXIMIZATION AND ASSOCIATED ACCURACY RATES

Region	$N=4$		$N=3$		$N=2$		$N=1$	
	Rate	$\lambda_0^{(m)}$	Rate	$\lambda_0^{(m)}$	Rate	$\lambda_0^{(m)}$	Rate	$\lambda_0^{(m)}$
Front	97.70	2	97.44	2	96.62	2	94.98	5
Left	96.72	2	95.98	2	95.76	2	93.02	5
Right	96.56	2	96.28	2	95.28	2	92.98	5
Far	90.04	3	89.24	5	87.40	4	85.74	10
Mean	95.25		94.74		93.76		91.68	

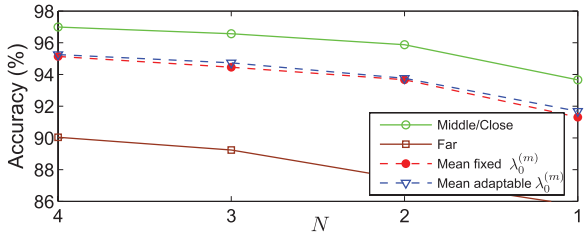

Fig. 7. Evolution of the accuracy of Gabor filters with adaptable $\lambda_0^{(m)}$ for the close/middle (green) and the far (brown) range as a function of the number of scales. The average accuracy evolution is also depicted (blue) and compared to that obtained for a fixed $\lambda_0^{(m)}$ (red). Observe that as a result of using an adaptable $\lambda_0^{(m)}$, the performance is enhanced for all N.

The advantage of characterizing each region of the image separately and of having a specific classifier for each of them becomes apparent in this case. Indeed, by appropriately choosing the best λ_0 we can obtain a nonnegligible gain in the correct classification rate. Table III summarizes the highest accuracy results for each region of the image (and the corresponding minimum wavelength $\lambda_0^{(m)}$) as a function of the image area. The average accuracy is enhanced compared to that obtained for a fixed λ_0 (Table II), with gains of 0.11%, 0.28%, 0.09%, and 0.37% for $N=4$, $N=3$ and $N=2$ and $N=1$, respectively. The final evolution of the performance as a function of the number of scales (broken down by zones), as well as the gain of using an adaptable λ_0 are shown in Fig. 7.

2) Performance as a Function of the Number of Orientations: Analogously to the number of scales, it is also interesting to analyze the evolution of the performance as a function of the number of orientations. Clearly, a minimum of $K=2$ orientations, i.e. vertical and horizontal, is mandatory, since those are highly present in vehicle images. We shall study the performance for $K=2, K=4$, $K=6$, and $K=9$, the angles ranging from 0 to $(K-1)/\pi K$ radians. The remaining parameters are chosen for performance maximization according to the experiments referred to above, i.e., $N=4$, $a=2$, $\lambda_0=2$ for the close/middle range, and $\lambda_0=3$ for the far range. The correct classification rates for the different numbers of orientation bins are given in Table IV. From the table, it is inferred that $K=6$ provides the best performance. Indeed, the use of $K=9$ instead of $K=6$ does not produce any remarkable gain (but rather a small average loss), therefore it does not justify the involved computational overhead. Inspection of the table also reveals that the performance decreases in average around 1.20% for $K=4$ with respect to $K=6$, while it plummets when decreasing K from 4 to 2.

TABLE IV

ACCURACY OF GABOR FILTERS AS A FUNCTION OF THE NUMBER OF ORIENTATIONS, K

Region	$K=9$	$K=6$	$K=4$	$K=2$
Front	97.98	97.70	97.50	95.22
Left	96.08	96.72	95.46	86.36
Right	96.80	96.56	94.98	86.70
Far	89.68	90.04	88.22	85.60
Mean	95.13	95.25	94.04	88.47

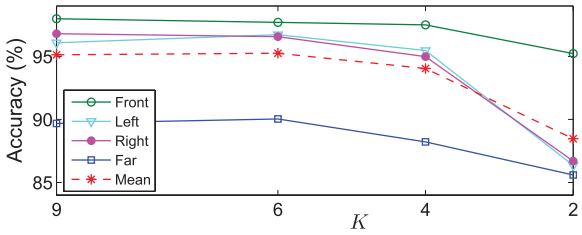

Fig. 8. Evolution of accuracy of Gabor filters as a function of K for the different image regions. The average evolution is also shown in red.

These results are illustrated in Fig. 8 in order to better grasp the underlying behavior. As can be observed, the highest performance degradation occurs in the left and right sides of the close/middle range when decreasing K to 2, i.e., only considering the vertical and horizontal orientations. This is mainly due to the fact the nonvehicle images in these regions contain structures in a whole bunch of angles, such as guardrails, median stripes, traffic signs, and lane markings, etc. These structures cannot be correctly captured with only 2 orientations, therefore the separability between vehicle and nonvehicle classes is reduced for $K=2$. This degradation is also observable, though less abruptly, for the far images, which also include some of these structures with a coarser detail. The decrease in performance is even more moderate for the front images, since fewer diagonal structures are to be observed in these region. A decrease from $K=6$ to $K=4$ results in an average small performance loss around 1.21%, which is larger in the left and right regions due to their richer diagonal content.

VI. PERFORMANCE OF LOG-GABOR FILTER-BASED CLASSIFIER

In this section, the goal is to experimentally compare the behavior of the proposed log-Gabor filter based descriptor with that of the traditional Gabor filter based approach used

TABLE V
ACCURACY OF LOG-GABOR FILTERS AS A FUNCTION OF THE NUMBER OF SCALES

$N=4$	$\lambda_0=2$	$\lambda_0=2.5$	$\lambda_0=3$	$\lambda_0=4$	$\lambda_0=5$
Front	98.00	97.78	97.20	97.68	96.84
Left	97.18	97.20	97.36	97.04	97.08
Right	96.96	97.06	96.90	96.64	96.64
Far	91.22	91.34	91.60	91.42	91.22
Mean	95.84	95.84	95.77	95.69	95.44

$N=3$	$\lambda_0=2$	$\lambda_0=3$
Front	97.36	97.18
Left	96.78	97.32
Right	96.94	96.40
Far	90.50	90.32
Mean	95.39	95.31

$N=2$	$\lambda_0=2$	$\lambda_0=4$	$\lambda_0=6$	$\lambda_0=8$
Front	97.54	97.08	96.50	95.58
Left	96.30	96.32	96.06	96.36
Right	96.30	96.40	95.92	95.68
Far	86.34	89.96	90.60	89.12
Mean	94.12	94.91	94.77	94.19

$N=1$	$\lambda_0=1$	$\lambda_0=5$	$\lambda_0=10$	$\lambda_0=15$	$\lambda_0=20$
Front	93.14	95.98	95.02	94.26	93.42
Left	90.02	95.90	95.94	94.36	92.94
Right	89.00	95.14	95.86	95.38	94.58
Far	72.84	84.00	86.54	86.98	85.44
Mean	86.25	92.76	93.34	92.75	91.60

TABLE VI
AVERAGE ACCURACY RESULTS OF LOG-GABOR FILTERS FOR DIFFERENT VALUES OF N FOR THE OPTIMAL FIXED λ_0

	$N=4$	$N=3$	$N=2$	$N=1$
Accuracy	95.84	95.39	94.91	93.34

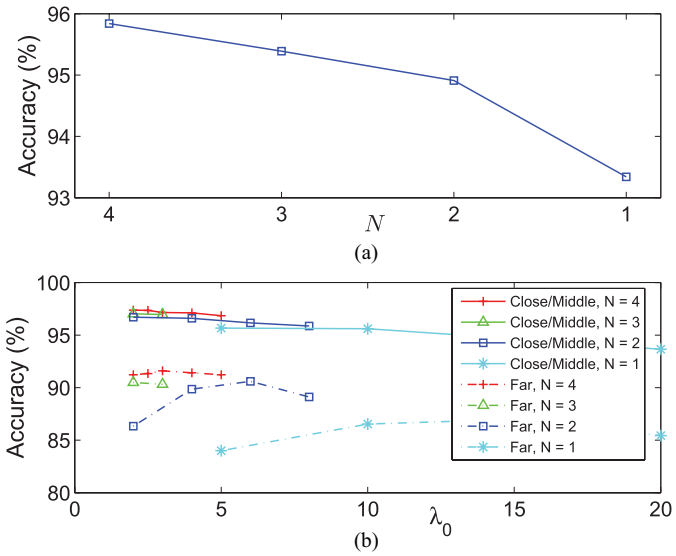

Fig. 9. Evolution of accuracy of log-Gabor filters as a function of N. (a) Average accuracy evolution. (b) Evolution as a function of the minimum wavelength λ_0 in the close/middle range (solid lines) and the far range (dashed lines).

in the state of the art, which has been analyzed in the previous section. The section is divided in three blocks. In Section VI-A, analogously to the Gabor functions, a set of simulations have been performed on the GTI vehicle database to evaluate the classification results when using log-Gabor functions and to find their appropriate parameter configuration. As explained, these filters have better properties in frequency than Gabor filters: namely, they adapt better to the response of visual neurons and achieve a larger and more efficient spectrum coverage. Section VI-B addresses the comparison between the results obtained for the proposed log-Gabor filter based descriptor with those of the state-of-the-art Gabor-based scheme evaluated in Section V. Finally, Section VI-C studies the performance of log-Gabor classifier with respect to other related methods in the state of the art.

A. Experiments With Log-Gabor Filter-Based Classifier

1) Performance as a Function of the Number of Scales: As done with the Gabor filters, different experiments are carried out by changing the number of scales from $N = 1$ to $N = 4$. The maximum frequency, F_0, and the scaling between center frequencies, a, are also adjusted so that the same range of frequencies $[0.05, 0.5]$ is covered. Remarkably, each filter of the log-Gabor bank can encompass a larger bandwidth than the traditional Gabor function, therefore theoretically a smaller impact in the performance is to be observed when decreasing the number of scales. In particular, the possibility to increase the bandwidth of log-Gabor filters is applied for $N \leq 3$ by decreasing β from 0.65 (approximately 1.5 octaves) to 0.55 (2 octaves). This allows in turn for an increase in the scaling between center frequencies ($a = 2$ for $N = 4$, $a = 3$ for $N \leq 3$), so that the desired range of frequencies can be approached. Table V contains the accuracy rates obtained from the tests. Table VI summarizes the rates obtained when the λ_0 yielding the best performance is selected for each value of N. The results in the tables confirm the expected average increase in performance obtained with log-Gabor filters with respect to Gabor filters.

In Fig. 9(a) the average performance evolution is displayed as a function of the number of scales N. As happened with the Gabor functions, the accuracy decreases quasi-linearly from $N = 4$ to $N = 2$, though with a smaller slope. Then the performance falls off more abruptly for $N = 1$. Also analogously to the Gabor functions, the λ_0 maximizing performance varies according to the image region, as shown in Fig. 9(b). Namely, the blurring in the far range images results in higher values of $\lambda_0^{(m)}$ than in the close/middle range, as explained in Section V-B. The best λ_0 for each image area and the accuracy rates obtained for each of them are summarized in Table VII, as well as the combined average rates.

The adaptation of $\lambda_0^{(m)}$ for each region of the image yields gains of 0.16%, 0.27% and 0.16% for $N = 4$, $N = 2$ and $N = 1$ (no gain is obtained for $N = 3$ as $\lambda_0^{(m)}$ remains the same for all regions of the image). The final evolution of the performance with respect to the number of scales for the close/middle and far ranges is shown in Fig. 10. The average enhancement obtained by using an adaptable (blue) instead of a fixed (red) $\lambda_0^{(m)}$ is also shown.

2) Performance as a Function of the Number of Orientations: The evolution of the classification performance achieved by using log-Gabor filters when varying the number of orien-

TABLE VII

VALUES OF λ_0 ADAPTED TO EACH IMAGE REGION FOR LOG-GABOR FILTER PERFORMANCE MAXIMIZATION AND ASSOCIATED ACCURACY RATES

Region	$N=4$		$N=3$		$N=2$		$N=1$	
	Rate	$\lambda_0^{(m)}$	Rate	$\lambda_0^{(m)}$	Rate	$\lambda_0^{(m)}$	Rate	$\lambda_0^{(m)}$
Front	98.00	2	97.36	2	97.54	2	95.98	5
Left	97.36	3	96.78	2	96.30	2	95.90	5
Right	97.06	2.5	96.94	2	96.30	2	95.14	5
Far	91.60	3	90.50	2	90.60	6	86.98	15
Mean	96.00		95.39		95.18		93.50	

TABLE VIII

ACCURACY OF LOG-GABOR FILTERS AS A FUNCTION OF THE NUMBER OF ORIENTATIONS, K

Region	$K=9$	$K=6$	$K=4$	$K=2$
Front	97.48	98.00	97.88	92.18
Left	97.10	97.18	95.90	83.40
Right	96.90	96.96	96.56	83.58
Far	91.22	91.60	88.68	83.94
Mean	95.67	95.94	94.75	85.77

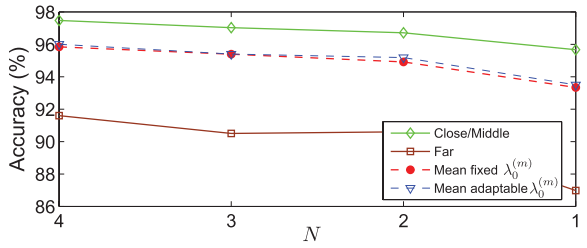

Fig. 10. Evolution of accuracy of log-Gabor filters with adaptable $\lambda_0^{(m)}$ for the close/middle (green) and the far (brown) range. The average accuracy evolution obtained for adaptable and fixed $\lambda_0^{(m)}$ are also depicted in blue and red, respectively.

TABLE IX

PERFORMANCE COMPARISON BETWEEN THE PROPOSED LOG-GABOR FILTER-BASED DESCRIPTOR AND THE GABOR FILTER-BASED DESCRIPTOR FOR OPTIMAL PARAMETERS

Method	Front		Left		Right		Far		Mean
	Rate	σ	Rate	σ	Rate	σ	Rate	σ	Rate
Gabor	97.70	0.23	96.72	0.25	96.56	0.37	90.04	0.52	95.25
Log-Gabor	98.00	0.24	97.36	0.18	97.06	0.24	91.60	0.28	96.00

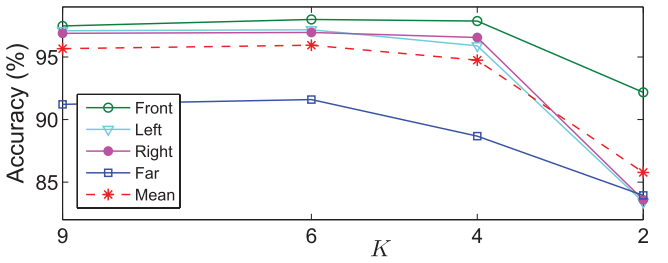

Fig. 11. Evolution of accuracy of log-Gabor filters as a function of K for the different image regions. The average evolution is also shown in red.

tations is analyzed in a similar manner to that of the Gabor filters. The remaining parameters are chosen for performance maximization: $N=4$, $a=2$ for all regions; $\lambda_0=2$ for the front close/middle range, $\lambda_0=2.5$ for the right close/middle region, and $\lambda_0=3$ for the left close/middle and far regions. Table VIII summarizes the accuracy rates obtained for the different orientation-wise configurations, which are in turn represented in Fig. 11. The best performance is achieved with $K=6$, and the effect of decreasing K is similar to that observed for Gabor filters: a small accuracy loss is produced when using only 4 orientations, whereas the use of only vertical and horizontal filters ($K=2$) reduces the performance dramatically, since modeling of the diagonal structures typical of nonvehicle images is not appropriately addressed. In the other side, $K=9$ over-discretizes the orientation space and leads to slightly worse results than $K=6$.

B. Comparison Between Gabor and Log-Gabor Based Classifiers

The performance of the descriptors using Gabor and log-Gabor functions is enclosed in Tables I to IV and Tables V to VIII, respectively. This is now summarized in Table IX, which compares the performance of the proposed log-Gabor filter based classifier with that based on the traditional Gabor filter used in the state of the art (as in approaches [13]–[15]). The rates obtained for the best configurations are shown for both methods (obtained from Tables III and VII, respectively). Observe that log-Gabor filter based descriptor results in an average gain of 0.75% with respect to the Gabor filter based descriptor. The table also contains the standard deviation, σ, of the mean accuracy obtained after repeating the experiment 10 times in order to show the statistical significance of the comparison. Note the small dispersion of the average accuracy, which is lower than the difference between the Gabor and the log-Gabor filter accuracy in all regions.

As discussed before, log-Gabor functions adapt better than Gabor functions to the inherent frequency content of natural images and are able to cover a larger spectrum with the same number of filters. Thus, it is especially interesting to observe their behavior when decreasing the number of filters in the bank, N. The rates obtained by varying N for both types of filters are visually illustrated in Fig. 12(a), both for a fixed $\lambda_0^{(m)}$ (Tables II and VI) and an adaptable $\lambda_0^{(m)}$ (Tables III and VII). Observe that the accuracy obtained with the descriptor using log-Gabor functions is significantly higher than that delivered by standard Gabor functions for all values of N. As stated, log-Gabor filters outperform Gabor filters for $N=4$ in around 0.7%, and the gap between them grows significantly as N decreases, which is in accordance with the expected behavior. Fig. 12(b) illustrates the performance gain when using log-Gabor filters instead of the traditional Gabor filters for feature extraction. Observe that the gain for a fixed $\lambda_0^{(m)}$ (red line) starts at 0.7 for $N=4$, grows softly for $N=3$, and keeps growing with an increasing slope for $N=2$ and $N=1$.

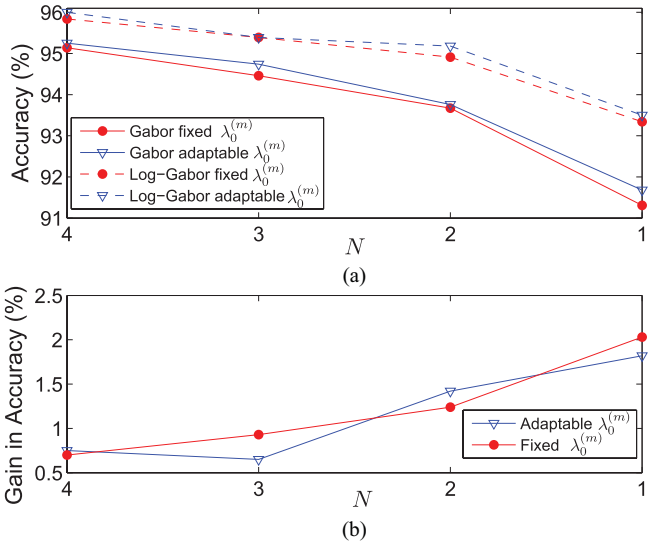

Fig. 12. Comparison of Gabor and log-Gabor classification performance. (a) Accuracy rates for Gabor (solid lines) and log-Gabor (dashed lines) both using a fixed $\lambda_0^{(m)}$ (red lines) and an adaptable $\lambda_0^{(m)}$ (blue lines). (b) Gain of using log-Gabor features instead of traditional Gabor filters is depicted.

As for an adaptable $\lambda_0^{(m)}$ (blue line), the enhancement obtained for Gabor filters for $N = 3$ allows to maintain the gap low, but it quickly shows the same ascending trend. These figures confirm the expected enhancement in performance of log-Gabor filters with respect to Gabor filters.

C. Log-Gabor Based Classifier Versus Other Methods

In the previous subsection, the superiority of the proposed log-Gabor filter based approach with respect to the traditional approach has been proven. However, it is also interesting to compare the performance of this method with respect to the other not Gabor-related state of the art approaches. In particular, as stated in Section I, the most widespread methods for vehicle verification, apart from Gabor filters, are Principal Component Analysis (PCA) and Histograms of Oriented Gradients (HOG). Table shows the comparison of these methods with the proposed log-Gabor filter based method in terms of accuracy. PCA features have been extracted by selecting the dimensionality d of the principal subspace yielding the maximum performance for each image region. These are $d = 40$ for the front close/middle region, and $d = 60$ for the left and right close/middle region and the far region. In turn, HOG features are extracted according to the original proposal by Dalal and Triggs [12], by also selecting the parameters, i.e., the cell size s, and the number of orientation bins β, which maximize the performance: $(s, \beta) = (4, 8)$ for the close/middle region, and $(s, \beta) = (8, 12)$ for the other regions. Naturally, the classification procedure, as well as the image database, is the same used for log-Gabor based descriptor (see Section V-A).

As can be observed, log-Gabor based approach (LG) outperforms PCA in all image regions. In turn, although HOG show an excellent performance, the computational requirements are very costly for real-time operation. In fact, the optimal configuration involves a feature vector of length $\beta\,(2\,(64/s-1))^2 = 7200$ for the front close/middle region and of 2352 for the other regions. This introduces an important computational overhead in the SVM classification stage. The average classification time (CT) in milliseconds required for each descriptor has been measured by means of the mySVM software [38] applied on the database images. As can be observed, the time required by HOG for classification is 8.04 ms, 17 times greater than that of LG. Considering a typical frame rate of 25 fps (40 ms per frame) and taking into account that other tasks of the processing chain as hypothesis generation and tracking generally consume most of the available time, the costly HOG verification is typically not affordable. Instead, the number of cells and/or orientation bins must be reduced in order to also reduce the feature vector and thus the classification time. For instance, the performance of using HOG with $(s, \beta) = (32, 8)$ in the front close/middle region and $(s, \beta) = (32, 12)$ in the other regions is also shown in the table (labeled as reduced-HOG). Observe that while the classification time is now comparable to that of PCA and LG, the average accuracy is lower than that of LG.

TABLE X
COMPARISON BETWEEN LOG-GABOR BASED APPROACH AND STATE-OF-THE-ART METHODS

Region	PCA		HOG		Reduced-HOG		LG	
	Rate	CT	Rate	CT	Rate	CT	Rate	CT
Front	96.22	0.28	99.18	15.32	95.36	0.30	98.00	0.24
Left	93.32	0.48	98.32	5.52	96.48	0.21	97.18	0.30
Right	91.04	0.60	97.44	5.65	95.64	0.21	96.96	0.23
Far	91.56	0.54	98.14	5.66	92.44	0.39	91.60	0.47
Mean	93.04	0.47	98.27	8.04	94.98	0.28	95.94	0.31

It is interesting to observe that, although the average performance of LG is better than that of the other methods, these also achieve outstanding rates (in some specific scenarios even higher than LG, e.g. reduced-HOG in the far region). This is due to the fact that each of them exploits information of different nature present in the original image. Hence, enhanced performance is expected by combining the different descriptors and classifiers. This will be the direction of our future research.

VII. CONCLUSION

In this study the potential of Gabor filters as descriptors for supervised vehicle classification has been assessed. First, the impact of the different design parameters of the Gabor-based descriptor has been evaluated in the field of vehicle imaging, yielding valuable conclusions. For instance, the optimal minimum wavelength of the filter bank, $\lambda_0^{(m)}$, is proven to be dependent on the pose of the vehicles, and in particular, to increase with the relative distance to them. Therefore, the descriptor has been designed with an adaptable $\lambda_0^{(m)}$, rendering a significant increase in performance with respect to a generic descriptor.

Most importantly, in contrast to typical approaches using Gabor filter banks, a new descriptor based on log-Gabor functions has been proposed. These functions have better theoretical properties than traditional Gabor filters for natural image representation, but had not been previously used for vehicle verification. The extensive experiments enclosed in this paper confirm the theoretical superiority of these filters over

Gabor filters in this field. In particular, log-Gabor filter banks are proven to yield better results than Gabor filter banks using the same number of filters due to their more effective coverage of the spectrum, and to scale better as the number of filters decreases.

REFERENCES

[1] Z. Sun, G. Bebis, and R. Miller, "On-road vehicle detection: A review," *IEEE Trans. Pattern Anal. Mach. Intell.*, vol. 28, no. 5, pp. 694–711, May 2006.

[2] C. Rotaru, T. Graf, and J. Zhang, "Color image segmentation in HSI space for automotive applications," *J. Real-Time Image Process.*, vol. 3, no. 4, pp. 311–322, Dec. 2008.

[3] L.-W. Tsai, J.-W. Hsieh, and K.-C. Fan, "Vehicle detection using normalized color and edge map," *IEEE Trans. Image Process.*, vol. 16, no. 3, pp. 850–864, Mar. 2007.

[4] C. Hoffmann, "Fusing multiple 2D visual features for vehicle detection," in *Proc. IEEE Intell. Veh. Symp.*, 2006, pp. 406–411.

[5] J. Hwang, K. Huh, and D. Lee, "Vision-based vehicle detection and tracking algorithm design," *Opt. Eng.*, vol. 48, no. 12, pp. 127201-1–127201-12, Dec. 2009.

[6] T. Wang, N. Zheng, J. Xin, and Z. Ma, "Integrating millimeter wave radar with a monocular vision sensor for on-road obstacle detection applications," *Sensors*, vol. 11, no. 9, pp. 8992–9008, Sep. 2011.

[7] K. Yamaguchi, A. Watanabe, and T. Naito, "Road region estimation using a sequence of monocular images," in *Proc. 19th Int. Conf. Pattern Recognit.*, 2008, pp. 1–4.

[8] J. Lou, T. Tan, W. Hu, H. Yang, and S. J. Maybank, "3-D model-based vehicle tracking," *IEEE Trans. Image Process.*, vol. 14, no. 10, pp. 1561–1569, Oct. 2005.

[9] Z. Zhang, T. Tan, K. Huang, and Y. Wang, "Three-dimensional deformable-model-based localization and recognition of road vehicles," *IEEE Trans. Image Process.*, vol. 21, no. 1, pp. 1–13, Jan. 2012.

[10] J. Zhou, D. Gao, and D. Zhang, "Moving vehicle detection for automatic traffic monitoring," *IEEE Trans. Veh. Tech.*, vol. 56, no. 1, pp. 51–59, Jan. 2007.

[11] T. Gandhi and M. M. Trivedi, "Video based surround vehicle detection, classification and logging from moving platforms: Issues and approaches," in *Proc. IEEE Intell. Veh. Symp.*, Jun. 2007, pp. 1067–1071.

[12] N. Dalal and B. Triggs, "Histograms of oriented gradients for human detection," in *Proc. IEEE Comput. Soc. Conf. Comput. Vis. Pattern Recognit.*, vol. 1. Jun. 2005, pp. 886–893.

[13] Z. Sun, G. Bebis, and R. Miller, "On-road vehicle detection using Gabor filters and support vector machines," in *Proc. 14th Int. Conf. Digit. Signal Process.*, vol. 2. 2002, pp. 1019–1022.

[14] Z. Sun, G. Bebis, and R. Miller, "Monocular precrash vehicle detection: Features and classifiers," *IEEE Trans. Image Process.*, vol. 15, no. 7, pp. 2019–2034, Jul. 2006.

[15] P. Dalka and A. Czyzewski, "Vehicle classification based on soft computing algorithms," in *LNCS*, vol. 6086. Jun. 2010, pp. 70–79.

[16] Y. Du and Y. Feng, "Vehicle detection from video sequence based on Gabor filter," in *Proc. Int. Conf. Electron. Meas. Instrum.*, Aug. 2009, pp. 375–379.

[17] H. Cheng, N. Zheng, and C. Sun, "Boosted Gabor features applied to vehicle detection," in *Proc. 18th Int. Conf. Pattern Recognit.*, 2006, pp. 662–666.

[18] J. Han and K.-K. Ma, "Rotation-invariant and scale-invariant Gabor features for texture image retrieval," *Image Vis. Comput.*, vol. 25, no. 9, pp. 1474–1481, Sep. 2007.

[19] B. S. Manjunath and W. Y. Ma, "Texture features for browsing and retrieval of image data," *IEEE Trans. Pattern Anal. Mach. Intell.*, vol. 18, no. 8, pp. 837–842, Aug. 1996.

[20] J. Melendez, M. Garcia, and D. Puig, "Efficient distance-based per-pixel texture classification with Gabor wavelet filters," *Pattern Anal. Appl.*, vol. 11, nos. 3–4, pp. 365–372, Sep. 2008.

[21] H. G. Jung, Y. H. Lee, P. J. Yoon, I. Y. Hwang, and J. Kim, "Sensor fusion based obstacle detection/classification for active pedestrian protection system," in *Proc. 2nd Int. Conf. Adv. Vis. Comput.*, 2006, pp. 294–305.

[22] J. Flusser and T. Suk, "Rotation moment invariants for recognition of symmetric objects," *IEEE Trans. Image Process.*, vol. 15, no. 12, pp. 3784–3789, Dec. 2006.

[23] S. E. Grigorescu, N. Petkov, and P. Kruizinga, "Comparison of texture features based on Gabor filters," *IEEE Trans. Image Process.*, vol. 11, no. 10, pp. 1160–1167, Oct. 2002.

[24] D. J. Field, "Relations between the statistics of natural images and the response properties of cortical cells," *J. Opt. Soc. Amer. A*, vol. 4, no. 12, pp. 2379–2394, Dec. 1987.

[25] J. G. Daugman, "Uncertainty relation for resolution in space, spatial frequency, and orientation optimized by two-dimensional visual cortical filters," *J. Opt. Soc. Amer. A*, vol. 2, no. 7, pp. 1160–1169, Jun. 1985.

[26] S. Fischer, G. Cristobal, and R. Redondo, "Sparse overcomplete Gabor wavelet representation based on local competitions," *IEEE Trans. Image Process.*, vol. 15, no. 12, pp. 3784–3789, Feb. 2006.

[27] T. P. Weldon, W. E. Higgins, and D. F. Dunn, "Gabor filter design for multiple texture segmentation," *Opt. Eng.*, vol. 35, no. 10, pp. 2852–2863, 1996.

[28] P. Kruizinga and N. Petkov, "Nonlinear operator for oriented texture," *IEEE Trans. Image Process.*, vol. 8, no. 10, pp. 1395–1407, Oct. 1999.

[29] X. W. Chen, X. Zeng, and D. V. Alphen, "Multi-class feature selection for texture classification," *Pattern Recognit. Lett.*, vol. 27, no. 14, pp. 1685–1691, Oct. 2006.

[30] R. Manthalkar, P. K. Biswas, and B. N. Chatterji, "Rotation invariant texture classification using even symmetric Gabor filters," *Pattern Recognit. Lett.*, vol. 24, no. 12, pp. 2061–2068, Aug. 2003.

[31] L. Cai, C. Ge, Y.-M. Zhao, and X. Yang, "Fast tracking of object contour based on color and texture," *Int. J. Pattern Recognit. Artif. Intell.*, vol. 23, no. 7, pp. 1421–1438, 2009.

[32] Z. Sun, G. Bebis, and R. Miller, "On-road vehicle detection using evolutionary Gabor filter optimization," *IEEE Trans. Intell. Transp. Syst.*, vol. 6, no. 2, pp. 125–137, Jun. 2005.

[33] J. Movellan, "Tutorial on Gabor Filters," MPLab Tutorials, UCSD MPLab, Tech. Rep., 2005.

[34] M. Nixon and A. Aguado, *Feature Extraction and Image Processing*, 2nd ed. New York, USA: Elsevier, 2008.

[35] S. Fischer, F. Šroubek, L. Perrinet, R. Redondo, and G. Cristóbal, "Self-invertible 2D log-Gabor wavelets," *Int. J. Comput. Vis.*, vol. 75, no. 2, pp. 231–246, Nov. 2007.

[36] P. Kovesi, "Image features from phase congruency," *Videre, J. Comput. Vis. Res.*, vol. 1, no. 3, pp. 1–26, 1999.

[37] *GTI Vehicle Image Database*. (2011) [Online]. Available: http://www.gti.ssr.upm.es/data/

[38] S. Rüping, "mySVM-Manual," Dept. Lehrstuhl Informatik, Univ. Dortmund, Dortmund, Germany, Tech. Rep., 2000.

Jon Arróspide Laborda received the Telecommunication Engineer degree from the TECNUN School of the Universidad de Navarra, San Sebastián, Spain, in 2006, and the Ph.D. degree (*summa cum laude*) from the E.T.S. Ingenieros de Telecomunicación, Universidad Politécnica de Madrid (UPM), Madrid, Spain, in 2012.

He was with the Fraunhofer Institut für Integrierte Schaltungen, Erlangen, Germany, from 2006 to 2007. Since 2007, he has been a member of the Grupo de Tratamiento de Imágenes (GTI, Image Processing Group), UPM. His current research interests include video analysis for object detection and tracking, especially related to intelligent transportation systems.

Luis Salgado received the Telecommunication Engineer and Ph.D. degrees in communications (*summa cum laude*) from the E.T.S. Ingenieros de Telecomunicación, Universidad Politécnica de Madrid (UPM), Madrid, Spain, in 1990 and 1998, respectively.

He has been a member of the Grupo de Tratamiento de Imágenes (GTI, Image Processing Group), UPM, since 1990. He was a Research Assistant from 1995 to 1996, and since 1996, he has been a Faculty Member of UPM, formerly as a Teaching Assistant, and currently as an Associate Professor (tenure in 2001) of signal theory and communications with the Department of Signals, Systems, and Communications. His current research interests include video analysis, processing and coding.

Dr. Salgado is an Associate Editor of the *Journal of Real-Time Image Processing*, has been a member of the Scientific and Program Committees of several international conferences and has been an Auditor and Evaluator of European research programs since 2002. He has participated in many national and international research projects.